FULL PAPER

Microstructure-Lattice Thermal Conductivity Correlation in Nanostructured PbTe$_{0.7}$S$_{0.3}$ Thermoelectric Materials

By *Jiaqing He, Steven N. Girard, Mercouri G. Kanatzidis,* and *Vinayak P. Dravid**

The reduction of thermal conductivity, and a comprehensive understanding of the microstructural constituents that cause this reduction, represent some of the important challenges for the further development of thermoelectric materials with improved figure of merit. Model PbTe-based thermoelectric materials that exhibit very low lattice thermal conductivity have been chosen for this microstructure–thermal conductivity correlation study. The nominal PbTe$_{0.7}$S$_{0.3}$ composition spinodally decomposes into two phases: PbTe and PbS. Orderly misfit dislocations, incomplete relaxed strain, and structure-modulated contrast rather than composition-modulated contrast are observed at the boundaries between the two phases. Furthermore, the samples also contain regularly shaped nanometer-scale precipitates. The theoretical calculations of the lattice thermal conductivity of the PbTe$_{0.7}$S$_{0.3}$ material, based on transmission electron microscopy observations, closely aligns with experimental measurements of the thermal conductivity of a very low value, $\sim$0.8 W m^{-1} K^{-1} at room temperature, approximately 35% and 30% of the value of the lattice thermal conductivity of either PbTe and PbS, respectively. It is shown that phase boundaries, interfacial dislocations, and nanometer-scale precipitates play an important role in enhancing phonon scattering and, therefore, in reducing the lattice thermal conductivity.

1. Introduction

Thermoelectric materials are among the important potential candidates for alternative and complementary sources for energy,

[*] Prof. V. P. Dravid, Dr. J. Q. He
Department of Materials Science & Engineering
Northwestern University
Evanston, IL 60208 (USA)
E-mail: v-dravid@northwestern.edu
Dr. J. Q. He, S. N. Girard, Prof. M. G. Kanatzidis
Department of Chemistry
Northwestern University
Evanston, IL 60208 (USA)
E-mail: m-kanatzidis@northwestern.edu
Prof. M. G. Kanatzidis
Materials Science Division
Argonne National Laboratory
Argonne, IL 60439 (USA)

wherein heat can be directly converted into electrical energy and vice versa.[1–4] These materials are realistic operational materials for applications in thermoelectric generators and refrigerators provided that they have, on average, a figure of merit, ZT, above $\sim$2.[5] The figure of merit is defined as ZT $= S^2\sigma T/\kappa$, where S, σ, κ, T, and $S^2\sigma$ are the Seebeck coefficient, electrical conductivity, thermal conductivity, absolute temperature, and power factor, respectively. Thermoelectric PbTe has a cubic structure and possesses promising thermoelectric properties and consequently has received considerable attention in the thermoelectric community for several decades.[6–8] However, although PbTe has good electrical transport properties, its overall figure of merit is not high enough mainly because of its relatively high lattice thermal conductivity.[9–11] Thus, there is considerable interest in understanding the influence of microstructure and inhomogeneity on lattice thermal conductivity in order to tailor PbTe for overall improved figure of merit.

With the aim of improving the efficiency of thermoelectric energy conversion, many efforts to increase the ZT have focused on increasing the Seebeck coefficient and electrical conductivity, while reducing thermal conductivity κ, which is the sum of the lattice, κ_{lat}, and the electronic, κ_{el}, contributions. Each parameter quantifies the heat-carrying efficiency of phonons for a given lattice, and of charge carriers, respectively. However, the challenge is to minimize the thermal conductivity while retaining desirable electronic transport properties. Therefore, a variation in carrier doping and lattice structure can significantly affect the optimization of the ZT values. Approaches to lowering the lattice thermal conductivity usually involve either inducing phonon scattering by impurity modes, or alloying the material (i.e., solid solution). However, alloying often adversely affects charge carrier scattering, and hence electrical resistivity rises to counteract the beneficial κ reduction.[12] In addition, solid solution alloying is not as effective at scattering high-energy acoustic phonons at elevated temperatures, thereby requiring alternative approaches to develop high-temperature thermoelectric materials. As an alternative, some researchers have developed new ways to introduce nanostructures

into the thermoelectric matrix, which results in much higher phonon scattering and thus lower lattice thermal conductivity. Many synthetic techniques have been proposed to insert these nanostructures; such as the fabrication of superlattices or quantum dots,[13–15] nanocrystalline inclusions,[16–24] and self-organization,[25,26] as well as formulating new structures.[27] For PbTe-based materials, high-performance nanostructured materials have been prepared through metallurgical processes, such as matrix encapsulation,[28] spinodal decomposition,[29] and nucleation and growth.[30]

Despite the formulation of numerous methods to reduce thermal conductivity, the underlying mechanism for lowering of the thermal conductivity is poorly understood. In this contribution, we present an experimental study of the PbTe–PbS system, which has low thermal conductivity, and explore the phenomenon of spinodal decomposition as a tool to produce nanostructured thermoelectric materials. We have investigated the nanometer-scale structures of $PbTe_{0.7}S_{0.3}$ by advanced transmission electron microscopy (TEM) and obtained unique insights as to their influence on lattice thermal conductivity.

2. Results

From the phase diagram of the $PbTe_{1-x}S_x$ system,[31] we find that $PbTe_{0.7}S_{0.3}$ has two possible phase states beneath the melting point: solid solution at high temperature ($\sim$970–1150 K); and spinodal decomposition at low temperature ($<$900 K). To investigate the morphology and microstructures of these two states, we have assessed two samples, SS = solid solution sample, and SD = sample with spinodal decomposition, by TEM.

Figure 1a is a low magnification image of sample SS that reveals a relatively homogenous contrast, except for some dark line-like features due to stacking fault defects. The electron diffraction pattern (inset) also does not show extra spots or distinctive spot splitting. However, in Figure 1b the high-resolution TEM (HRTEM) image of the solid solution $PbTe_{0.7}S_{0.3}$ depicts many particles with weak contrast with a size of $\sim$1 nm, some of which are indicated by arrowheads and circles in the figure. This is indicative of a possible nanostructured pseudo-solid solution or the early stage of spinodal decomposition. To verify and confirm the spinodal decomposition, the sample was studied by in situ heating in the TEM to 600 °C, at rate of 10 °C min^{-1}. Figure 1c is a bright field (BF) image of the sample at 500 °C that depicts one modulated structure marked A (details are discussed later), and at least two different regions are observed. Figure 1d is the electron diffraction pattern with a single selected area aperture covering the two areas which shows that there are two distinct sets of diffraction patterns that likely arise from two different but coherent phases.

Figure 2a is the low magnification BF image of sample SD that also shows two types of contrast, marked as A and B. Figure 2b is the electron diffraction pattern taken from the A/B boundary. The diffraction pattern shows the coherency between PbTe and PbS that is apparent as a single crystal diffraction pattern with an orientation relationship of $(001)_{PbTe}||(001)_{PbS}$. The lattice mismatch at room temperature between the PbTe and PbS is about 6%; calculated using $(a_{PbTe} - a_{PbS})/a_{PbTe}$, a value which is consistent with the measured data from our electron diffraction.

Elemental maps were collected using energy X-ray dispersive spectroscopy (EDS) in the scanning transmission electron
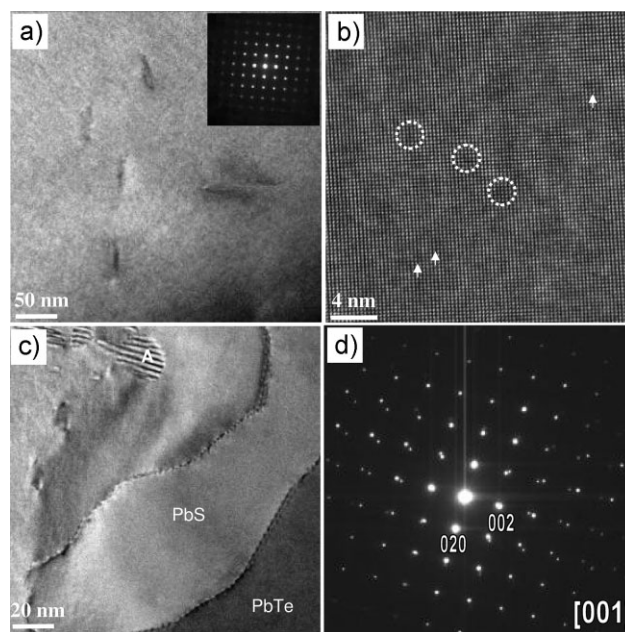

Figure 1. a) Low-magnification image and electron diffraction (inset) show homogenous contrast except for some dark lines from defects. However b) the HRTEM lattice image shows inhomogeneous weak contrast particles about 1 nm in size. c) Heating the sample in situ to 500 °C reveals spinodal decomposition into two regions with different contrasts, one typical modulated structure is labeled by the letter A. d) Electron diffraction pattern with the aperture including the two different regions of contrast.

microscopy (STEM) mode using a $\sim$1 nm probe size to further confirm the composition of the two phases. Figure 2c is the low magnification dark field (DF) STEM image, which clearly shows the different contrast of the two phases. The compositional line scan from A to B (in Fig. 2c) is plotted in Figure 2d. The relative counts of S are higher in the C region than in the D region, while the reverse is the case for Te. The Pb element appears in all the regions, but the counts are a little higher in the C region than in the D region because the former region is thicker as a result of dissimilar ion-milling rates during the preparation of the TEM sample. Spectrum imaging in Figure 2e confirmed these results. The elemental mapping reveals the presence of Pb and S in the C region, and Pb and Te in the D region. While the counts of Pb are not very uniform crossing the two regions; the counts of Te and S complement each other in both. Thus, comparison of these data with the electron diffraction pattern in Figure 2b confirms the identity of PbS and PbTe in region C and D, respectively.

Because of the large lattice mismatch of about 6% between PbTe and PbS, there is considerable expected lattice strain at the PbTe/PbS boundaries. The TEM observations reveal the presence of regular misfit dislocations (Fig. 3), a small distorted region (Fig. 4), and structural modulations (Fig. 5). Figure 3a is a HRTEM image with Moiré fringes of the PbTe/PbS boundary. The image shows a series of misfit dislocation cores at the boundary. Image processing[26,32] has been employed to investigate the strain variation of dislocation cores at/around this boundary in the image. In Figure 3b, the power spectrum of the image in Figure 3a, reciprocal vectors $g_1 = 02\bar{2}$ and $g_2 = 20\bar{2}$ were chosen as the Fourier
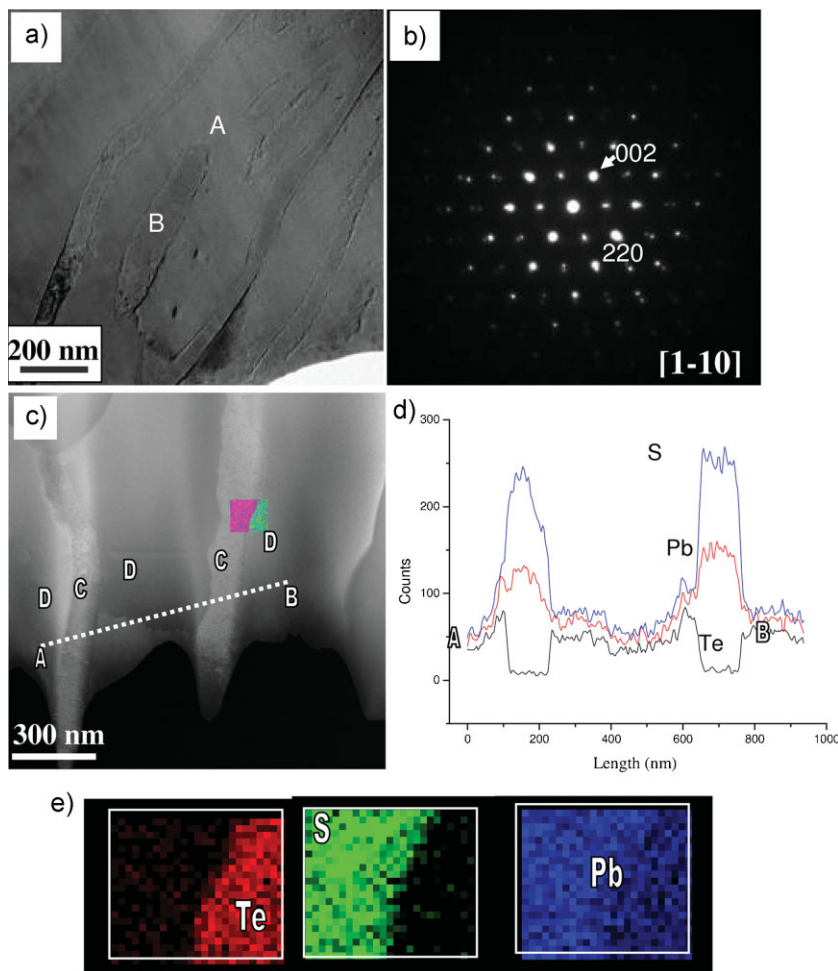
Figure 2. a) Low-magnification bright-field image of a PbTe$_{0.7}$S$_{0.3}$ sample, clearly showing two contrasting areas, marked A and B. b) Selected electron diffraction patterns taken from the A/B boundary. c) Low-magnification STEM image showing regions of PbS (labeled C) and PbTe (labeled D). d) EDS line scan from A to B in (c) shows Te and S are complementary to each other, while the counts of Pb are non-uniform in two regions due to the crystal's inhomogeneous thickness. e) Further confirmation from spectrum imaging. The element mapping clearly shows the elements Pb and S in the C region, and Pb and S in the D region. Comparing this with the electron diffraction patterns in (b), PbS and PbTe are identified in regions C (B) and D (A), respectively.

indexes the positions of the dislocation cores. Figure 3g is the enlarged part of region A in Figure 3e, The Burger's circuit around the dislocation core yields a closure failure with a projected vector $\frac{1}{2}a[100]$. Although the vector is not a lattice-translation vector, other $\frac{1}{2}a[100]$ dislocations are present nearby. This finding means that the misfit dislocation $a[100]$ usually has dissociated into two partial ones with Burger's vectors $\frac{1}{2}a[100]$, and that the two partials are related by a stacking fault or an antiphase boundary between them. According to Frank's rule,[33] the observed dissociation reaction is energetically favorable. Figure 3h illustrates the results of modeling and simulation of this type of edge dislocation. The image is calculated on the basis of a computer model constructed by the iterative procedure. The arrowheads point to the extra semi-atomic plane. The simulated image agrees quite well with the experimental image and suggests that white dots in the image are atomic columns.

The atomic resolution image of another PbTe/PbS boundary is depicted in Figure 4a. The misfit dislocations are still apparent; however, the spacing between them is slightly larger than the calculated figure because of the incomplete relaxation of the strain. Figure 4b illustrates the variation of the out-of-plane lattice parameter with depth, measured from the PbTe/PbS boundary, and represented in unit cells from cation positions calculated by direct lattice mapping on this HRTEM image. For this purpose, we applied a numerical center-of-mass approach (the crosses marking location of atoms in Fig. 4b) taking the out-of-plane PbS lattice parameters as the calibration standard. The results of this analysis, which appear in Figure 4c, reveal that the lattice parameter of PbTe is around 6.4 Å, while in the boundary region (within about 2.5 nm), the lattice parameters continuously fall from 6.4 to 5.9 Å. These observations suggest that some strain at the boundary is not completely relaxed.

vectors for strain analysis. The profile of the strain map along the in-plane direction (ε_{xx}) is given in Figure 3c, which displays orderly dislocation cores and about a 6% displacement from PbTe to PbS. In an alternative depiction in Figure 3d, the magnitude of the displacement is represented by a contour map that unambiguously confirms the difference between the two phases and dislocation cores at the boundary. We have noted a regular spacing of about 2 nm among the dislocation cores (the density of dislocation in the sample is $\sim 2.5 \times 10^{12}$ cm^{-2}). Because the observed value is slightly higher than calculated (~ 1.7 nm), we believe it suggests that the misfit strain is not completely relaxed at the boundary.

Figure 3e is a HRTEM image of the PbTe/PbS boundary close to the edge of the sample hole. The circles highlight the dislocation cores. Its inverse fast Fourier transform (IFFT) in Figure 3f clearly

Figure 5a is a low-magnification HRTEM image of the PbTe/PbS boundaries, wherein we note two types of modulated structures, labeled A and B. One (A) with unidirectional modulation is shown at high magnification in Figure 5b; another one is shown in Figure 5c. Here, the modulation is three directional, as seen in the pseudo-hexagonal pattern. Figure 5d is a typical electron diffraction pattern (EDP) generated by a single selected area aperture including PbTe, PbS, and the secondary modulated structure boundary. In this diffraction pattern the electron beam enters PbTe and exits from PbS. We note that all the spots in this diffraction pattern are split. Interestingly, these spots have quite different characteristics from those shown in Figure 2b, i.e., they cannot be obtained by simply superimposing the electron diffraction patterns of PbTe [001] and PbS [001] zones. As seen in Figure 5d, it has many more split spots than those in Figure 2b.
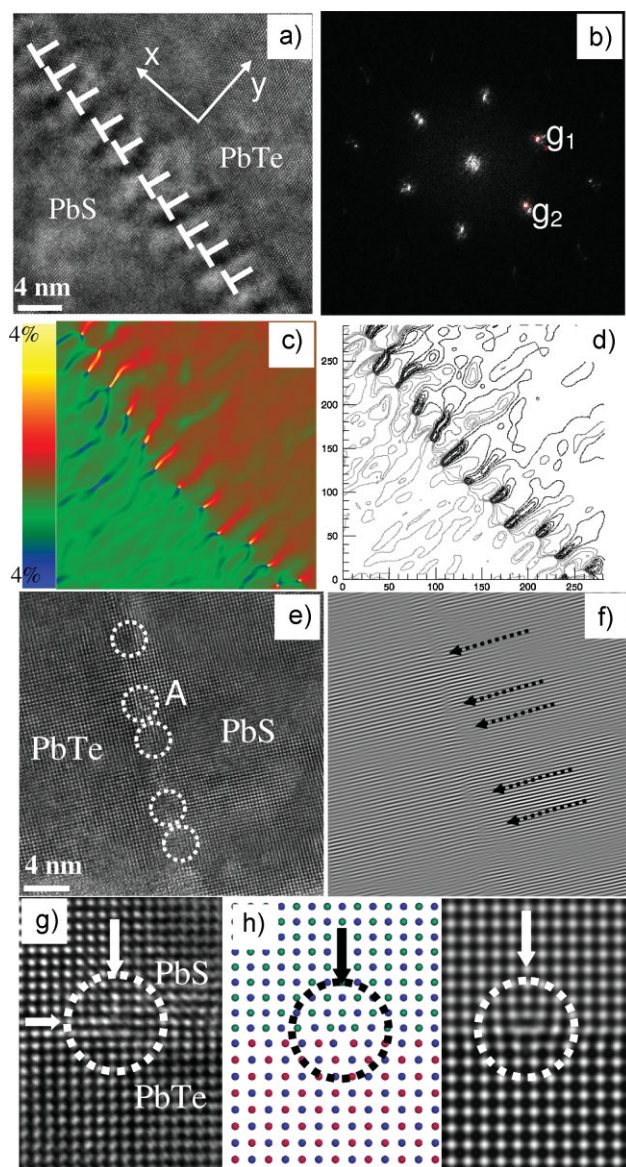
www.MaterialsViews.com

ADVANCED
FUNCTIONAL
MATERIALS
www.afm-journal.de

FULL PAPER

Figure 3. a) The HRTEM image of the PbTe/PbS boundary with Moiré fringes. b) Power spectrum plot of image (a), the two vectors g_1 and g_2 were selected for image processing. c) Strain mapping of image (a) shows the dislocation cores in the high-intensity short lines. d) The magnitude of the displacement depicted as a contour map. e) The lattice image of the PbTe/PbS boundary in the very thin regions shows some dislocations encircled in white. f) The IFFT image depicts the additional semi-atomic planes (pointed by arrows) at the dislocation core of the PbS side. g) High-magnification image from region A in image (e) includes one clear dislocation core with a Burgers vector of $\frac{1}{2}$[100]. h) The atomic model of this dislocation, and its simulation lattice image.

Furthermore, this is a complicated pattern similar to that observed in some incommensurate or commensurate-modulated structures.[34,35] Figure 5e is the enlarged split-spot indexed as ($\overline{4}22$) in Figure 5d. The diffraction spots in Figure 5e were obtained due to double diffraction of the PbTe [111] and PbS [111] zones; the reciprocal lattice vector g_{hkluvw} of such a diffraction spot is
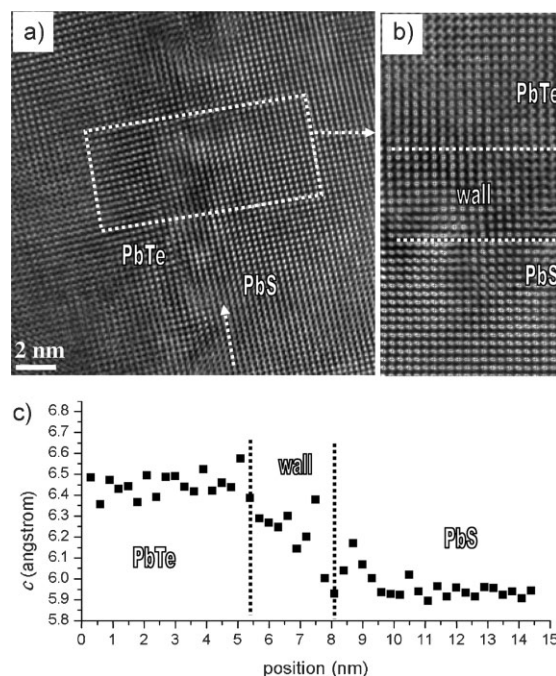

Figure 4. a) Atomic-resolution image of the near-PbTe/PbS interface region with the zone axis along 100_{PbTe} direction. The white arrow points to the interface. b) The digital region from the boxed area of the image in (a). c) Evolution of the out-of-the-plane lattice parameters with depth along the out-of-the-plane direction, revealing that the boundary about 2.5 nm is strained.

expressed by:

$$g_{hkluvw} = ha^*_{PbTe} + kb^*_{PbTe} + lc^*_{PbTe} + ua^*_{PbS} + vb^*_{PbS} + wc^*_{PbS} \qquad (1)$$

Where h, k, l, u, v, and w are all integers, a^*_{PbTe}, b^*_{PbTe}, and c^*_{PbTe} are unit vectors of PbTe in the reciprocal space, and a^*_{PbS}, b^*_{PbS}, and c^*_{PbS} correspond to the reciprocal unit vectors of PbS. We can then index the diffraction spots in Figure 5e using six indices ($hkluvw$). For example, diffraction spots 1 and 2 in Figure 5e are indexed using ($000\overline{4}22$) and ($\overline{4}22000$), respectively; Table 1 summarizes the indices of all of the marked diffraction spots. The diffraction spots with ($hkl000$) indices correspond to PbTe, while those with ($000uvw$) correspond to PbS. The diffraction spots with ($hkluvw$) (h, k, l, u, v, and w are nonzero integers) correspond to the double-diffraction spots. Figure 5f is the simulated electron-diffraction pattern based on PbTe and PbS with a double-diffraction effect, which is quite similar to the experimental electron diffraction pattern in Figure 5d. In Figure 5f the spots represent the diffraction spots from PbTe, PbS, and double diffractions.

Besides the dislocations and small remaining strain at the PbTe/PbS boundary, many nanometer-scale sphere and plate-like precipitates were detected in most PbS features and in some regions of the PbTe matrix. Figure 6a is a typical low magnification image that has several precipitates in the PbS area. From high magnification images, some nanometer-scale precipitates were determined to be plate-like. As a result, in the lattice images such as Figure 6b, the plate-like precipitates show a straight-line-like
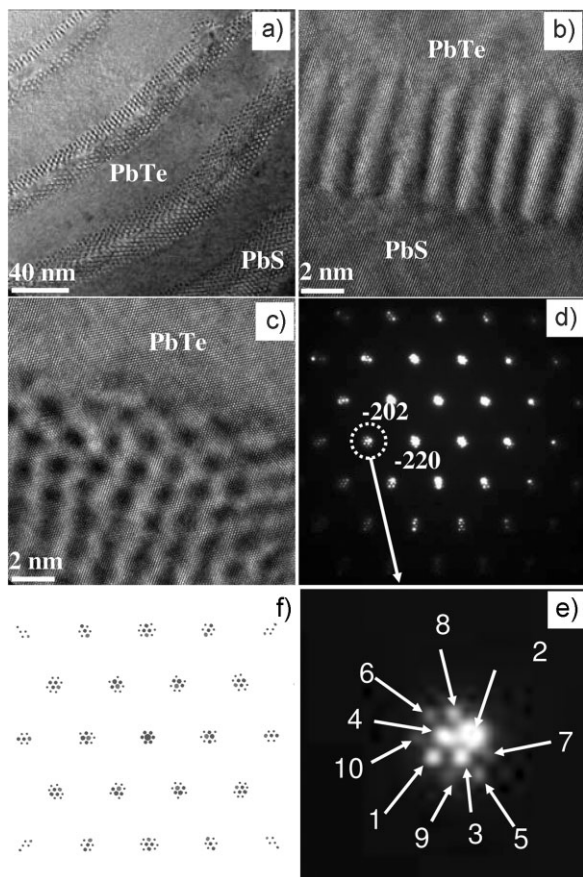
**ADVANCED
FUNCTIONAL
MATERIALS**
www.afm-journal.de

Materials Views
www.MaterialsViews.com

Figure 5. a) The low-magnification HRTEM image of PbTe/PbS boundaries, showing two types of modulated structures. b) A high-magnification image of a unidirectional modulated structure evidenced by the straight-line patterns, and c) high-magnification images of a modulation along three directions evidenced through the hexagonal patterns. d) Electron-diffraction pattern generated by one select area aperture from (c), including PbTe, PbS, and the modulated structure boundary, shows that all the spots are split. e) The enlarged split spot marked by a circle in (d). f) The simulated electron diffraction pattern of PbTe and PbS including double diffraction.

Table 1. Indices (*hkluvw*) of the marked diffraction spots in Figure 5e.

Number	Indices
1	$(000\bar{4}22)$
2	$(\bar{4}22000)$
3	$(\bar{2}02\bar{2}20)$
4	$(\bar{2}20\bar{2}02)$
5	$(\bar{2}\bar{2}4\bar{2}4\bar{2})$
6	$(\bar{2}4\bar{2}\bar{2}2\bar{2}4)$
7	$(\bar{4}0402\bar{2})$
8	$(\bar{4}40\bar{0}2\bar{2})$
9	$(02\bar{2}404)$
10	$(0\bar{2}\bar{2}440)$

contrast, and square contrast in the orthogonal direction as seen in the insert. Figure 6c is the schematic representation of this system highlighting the nanocrystals of the plate-like precipitates. The two images in Figure 6b correspond to the two orthogonal directional

views of Figure 6c. The estimates of the distribution density and average size of all types of nanometer-scale precipitates are, $\sim 1 \times 10^{12}$ cm^{-2} and ~ 3 nm, respectively.

3. Discussion

In Figure 7a–d the electrical transport properties of the three samples: PbTe, the solid solution PbTe$_{0.7}$S$_{0.3}$ sample (SS), and the spinodal decomposition PbTe$_{0.7}$S$_{0.3}$ sample (SD), are compared. While the temperature-dependent properties of the SD sample can be easily measured, any high-temperature measurement of a SS sample will immediately result in phase separation as dictated by the thermodynamics of spinodal decomposition; thus comparison of room-temperature properties provides a clear view of the change in transport.[31] The measured room-temperature electrical conductivity of the SS sample is approximately 1300 S cm^{-1}, which is reduced to a room-temperature value of electrical conductivity of 900 S cm^{-1} following decomposition (Fig. 7a). Figure 7b shows that a slight increase in thermopower is observed at room temperature following phase separation, from -120 to -100 μV K^{-1}. The significant reduction in electrical conductivity following phase separation would suggest that the decomposition of large regions of PbS throughout the thermoelectric matrix might significantly degrade electrical transport in the material. The decomposed PbS features in the SD material exhibits misfit locations, incompletely relaxed strains, and a wide range of particle sizes that effectively reduce the electrical conductivity as a result of electron scattering. The spinodal decomposition phase transformation may also help to remedy point defects and vacancies that form within the crystal structure of the material following rapid solidification, which may also contribute to changes in both electrical conductivity and thermopower as a result of fluctuations in carrier concentration.

Phase separation moving from SS to SD in the samples results in a net increase in total thermal conductivity, from approximately 1 to 1.2 W m^{-1} K^{-1} (Fig. 7c). The corresponding value for the lattice thermal conductivity is very low for the SS sample, approximately 0.2 W m^{-1} K^{-1} at room temperature, which steadily increases at higher temperatures (Fig. 7d). It is understood that for a spinodal decomposition process, even rapidly cooled samples will be immediately unstable; this results in small particles or periodic compositional fluctuations that will continue to decompose and form the characteristic spinodally decomposed microstructure given increased time or temperature.[36] We have verified the presence of these structures in Figure 1. It is apparent here that the presence of these features is quite effective in reducing the lattice thermal conductivity. However, given the unstable nature of the SS sample, it will naturally and irreversibly decompose to the SD material, as seen in Figure 2. The resulting lattice thermal conductivity for the thermodynamically stable SD sample is approximately 0.6 W m^{-1} K^{-1} over the entire temperature range. Following decomposition, repeated high temperature cycling will not alter the thermoelectric properties, which indicates the material has reached thermodynamic equilibrium. While the values of lattice thermal conductivity are quite low, especially for the SS sample, our results are consistent with experimentally derived values of a number of other nanostructured materials.[29,37,38]
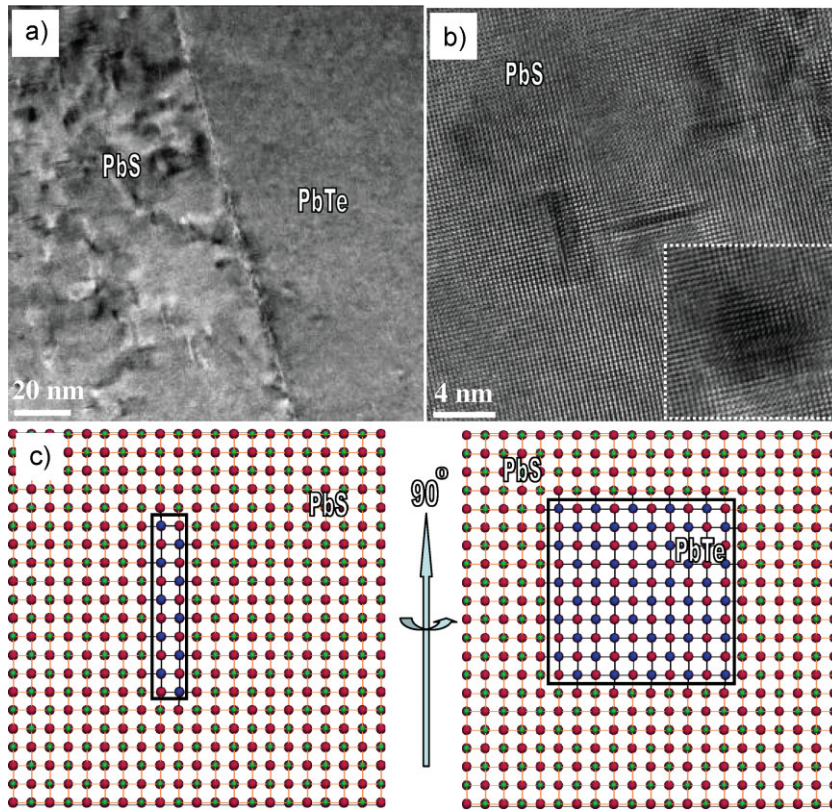
Figure 6. a) Low-magnification image showing nanometer-scale precipitates. b) The high magnification images show the straight-line and square-like (inset) contrasts, which indicates that the precipitates are plate-like in shape. c) The modeling of the nanometer-scale straight-line-like precipitates; their appearance in one direction is line-like, but after a 90 degree rotation, a square emerges.

To clarify the possible mechanisms in reducing the lattice thermal conductivity of the SD sample (for example, the roles of boundaries, strains, precipitates, and dislocations), we calculated the lattice thermal conductivity based on our TEM observations using the Callway's model:[39]

$$\kappa_l = \frac{k_B}{2\pi^2 \upsilon}\left(\frac{k_B T}{\hbar}\right)^3 \int_0^{\theta_D/T} \tau_c(x)\frac{x^4 e^x}{(e^x-1)^2}\,\mathrm{d}x \quad (2)$$

where k_B is the Boltzmann's constant, $\hbar$ is the Plank constant, T is the absolute temperature, υ is an average phonon-group velocity, which can be calculated from $\upsilon^{-1} = \frac{1}{3}\left(\upsilon_{T,1}^{-1} + \upsilon_{T,2}^{-1} + \upsilon_L^{-1}\right)$, where υ_L and $\upsilon_{T,1,2}$ are the longitudinal- and transverse-sound velocity, respectively; $x = \hbar\omega/\kappa_B T$, and τ_c is the relaxation time. The latter is obtained by integrating the relaxation times from various processes. In the TEM studies, at a certain frequency, the relaxation time mainly is related to scattering from the boundaries, dislocations, strains, nanometer-scale precipitates, and the phonon–phonon interactions;[39]

$$\frac{1}{\tau_c} = \frac{1}{\tau_U} + \frac{1}{\tau_N} + \frac{1}{\tau_{SD}} + \frac{1}{\tau_S} = \frac{1}{\tau_U} + \frac{1}{\tau_N} + \frac{1}{\tau_B} + \frac{1}{\tau_D} + \frac{1}{\tau_P} + \frac{1}{\tau_S} \quad (3)$$

where τ_U, τ_N, τ_{SD}, τ_S, τ_P, τ_B, and τ_D, are the relaxation times[40–48] that correspond to scattering from Umklapp processes, normal processes, spinodal decomposition, strains, precipitates, boundaries, and dislocations, respectively. In principle, more mechanisms may further contribute to the relaxation time, such as electron–phonon interactions. In our treatment, however, we consider only the six main contributors.

From the second-order perturbation theory, the relaxation time for Umklapp scattering is given by:[40]

$$\tau_U^{-1} \approx \frac{\hbar\gamma^2}{M\upsilon^2\theta_D}\omega^2 T \exp(-\theta_D/3T) \quad (4)$$

wherein γ is the Gruneisen anharmonicity parameter, M is the average mass of an atom in the crystal, and θ_D is the Debye temperature.

For normal phonon–phonon scattering, several models were proposed.[40–42] The appropriate form of group IV or III–V semiconductors can be written as:[40]

$$\tau_N^{-1} \approx B_N \omega^a T^b \quad (5)$$

where depending on the type of phonons, $(a, b) = (1, 4)$ for longitudinal phonons, and $(a, b) = (2, 3)$ transverse phonons, B_N is a constant independent of ω and T, $B_N(1,4) \approx \frac{k_B^4\gamma^2 V_0}{Mh^3\upsilon^5}$, $B_N(2,3) \approx \frac{k_B^3\gamma^2 V_0}{Mh^2\upsilon^5}$; and V_0 is the volume per atom. Some researchers have also given τ_N by:[41,42]

$$\tau_N^{-1} \approx \beta\tau_U^{-1} \quad (6)$$

where β is the ratio of normal phonon scattering to Umklapp scattering, which is assumed to be temperature independent. Here we used Equation 6 to calculate normal phonon scattering of our study. The value of parameter β will be determined by fitting experimental data of pure PbTe.

Interfaces and boundaries change the crystal's spring stiffness (or acoustic impedance), inducing it to scatter phonons. This is similar to the scattering of electromagnetic waves in the presence of a change in the optical refractive index. Since the images in Figure 2a, 4a, and 5a are quite similar to the superlattice, we treat these boundaries as an effective superlattice. The relaxation time is then written as:[43,44]

$$\tau_B^{-1} = \frac{\upsilon(1-t)}{L\left(\frac{3}{4}t\right)} \quad (7)$$

wherein $t = \frac{1}{2}(t_{12} + t_{21})$, an average phonon transmissivity at the interface, is estimated by $t_{12} = U_2\,\upsilon_2/(U_1\,\upsilon_1 + U_2\,\upsilon_2)$; here, t_{12} is the phonon transmissivity from medium 1 to 2, and U is the
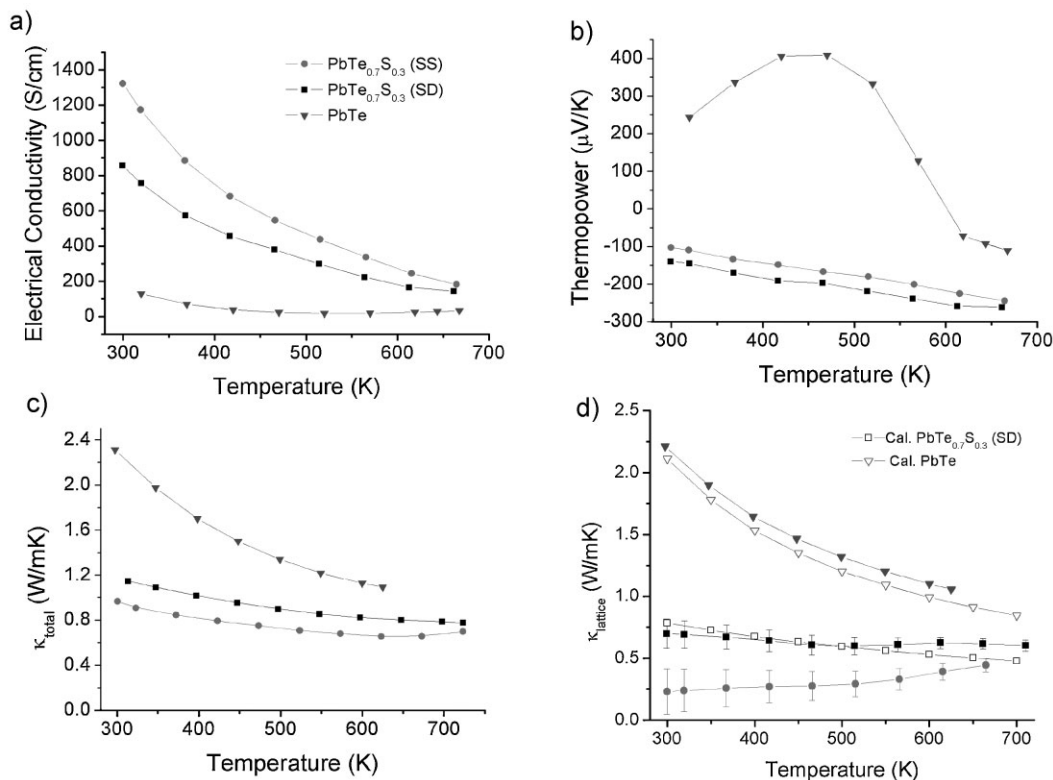
Figure 7. a) Electrical conductivity, b) thermopower, c) total thermal conductivity, and d) lattice thermal conductivity dependence of the temperature of PbTe, solid solution $PbTe_{0.7}S_{0.3}$ (SS), and spinodal decomposition $PbTe_{0.7}S_{0.3}$ (SD). In (d), the calculated lattice thermal conductivity based on TEM observations (open triangles and squares), is compared with experimental values (closed squares and circles). The error bars show plus and minus one standard deviation in the experimental determination of the lattice thermal conductivity, assuming a range of Lorenz numbers explained in the text.

density of the phonon energy (note $= v^2\rho$), and L is the segment length, about 120 nm in our sample SD by TEM.

In addition to the boundary scattering mechanism, scattering due to dislocations are incorporated into the relaxation time according to our observations. We use here the following simplified dislocations:[45]

$$\tau_D^{-1} = N_D \frac{V_0^{4/3}}{v^2} \omega^3$$
$$+ 0.06 N_D \gamma^2 B_D^2 \omega \left\{ 1/2 + \frac{1}{24} \left(\frac{1-2v}{1-v} \right)^2 \left[1 + \sqrt{2} \left(\frac{v_L}{v_T} \right)^2 \right]^2 \right\} \tag{8}$$

where N_D is the dislocation density, r is the core radius, B_D is the magnitude of the Burgers vector of the dislocation, γ is the Gruneisen number, and ω is the phonon angular frequency. The first term in this equation is the contribution of the dislocation core, and the secondary term is due to the surrounding strain field. Since PbTe and PbS are anisotropic structures, we use the approximation of averaged elastic constants with the anisotropic factor, H, defined over the elastic coefficients c_{ij} by $H = 2c_{44} + c_{12} - c_{11}$, the averaged elastic constant λ, and shear modulus μ for a cubic crystal are $\lambda = c_{12} - (1/5)H$ and

$\mu = c_{44} - (1/5)H$, correspondingly. The Poisson's ratio v is equal to $\frac{\lambda}{2(\lambda+\mu)}$.

The TEM observations have revealed abundant precipitates in the SD sample. Relaxation time of phonon scattering due to the nanometer-scale precipitates is given by a Mathiessen-type interpolation between the short- and long-wavelength scattering regimes:[46–48]

$$\tau_P^{-1} = v(\sigma_s^{-1} + \sigma_l^{-1})^{-1} V_p \tag{9}$$

where $\sigma_s = 2\pi R^2$; $\sigma_l = \pi R^2 \frac{4}{9} (\Delta D/D)^2 (\omega R/v)^4$, here R is the particle average radius; D is medium density, and ΔD is the difference between the particle and matrix materials; V_p is the density of the nanometer-scale particles.

Based on these formulae and the parameters in Table 2, we have calculated the lattice thermal conductivity of pure PbTe (note that to better fit the experimental data of pure PbTe we also included the small contributions of dislocations and grain boundaries based on TEM observations) and nanostructured $PbTe_{0.7}S_{0.3}$. In order to compare the reliability of the calculations, we directly compare the lattice thermal conductivity of our calculated values to experimentally derived values for $PbTe_{0.7}S_{0.3}$, as plotted in Figure 7d.[31] Under the margin of error, the agreement between the calculated and experimental data for the $PbTe_{0.7}S_{0.3}$ sample in Figure 7d

www.MaterialsViews.com

ADVANCED
FUNCTIONAL
MATERIALS
www.afm-journal.de

FULL PAPER

Table 2. Parameters used to calculate the lattice thermal conductivity, taken from our calculations or ref. [7]. PbTe$_{0.7}$S$_{0.3}$ was calculated based on the volume fraction of the two phases.

Parameters		PbTe	PbS
Lattice constant	a [Å]	6.460	5.936
Elastic coefficients	c_{11} [GPa]	105.3	127
	c_{12} [GPa]	7.0	29.8
	c_{44} [GPa]	13.2	24.8
	H [GPa]	−71.9	−47.6
	λ [GPa]	21.4	39.32
	μ [GPa]	27.6	34.32
	ν	0.218	0.267
Volume per atom	V_0 [Å^3]	33.69	26.15
Gruneisen parameter	γ	1.96	2.52
Longitudinal sound velocity	υ_L [m s^{-1}]	3590	4080
Transverse sound velocity	$\upsilon_{T,1}$ [m s^{-1}]	1260	1480
Transverse sound velocity	$\upsilon_{T,2}$ [m s^{-1}]	1610	1840
Polarization sound velocity	υ [m s^{-1}]	1770	2040
Debye temperature	θ_D [K]	136	145
Energy transmissivity	t	0.629	0.371
Density of mass	ρ [g cm^{-3}]	8.242	7.597

reinforces the validity of our argument, i.e., that boundaries, dislocations, and nanometer-scale precipitates significantly reduce the lattice's thermal conductivity. All of these microstructural features lower the lattice thermal conductivity of PbTe$_{0.7}$S$_{0.3}$ well below that of pure PbTe. Although somewhat intuitively obvious, this contribution provides a comprehensive account that reflects the consistency between experimental observations and theoretical basis.

4. Conclusions

The detailed microstructure of thermoelectric PbTe$_{0.7}$S$_{0.3}$ specimens has been examined by advanced TEM in the context of its influence on the thermoelectric figure of merit; specifically with respect to the thermal conductivity. The study reveals that dislocations, boundaries, and especially nanometer-scale particles/precipitates associated with spinodal decomposition play a key role in increasing phonon scattering thus reducing the lattice thermal conductivity of this system. The theoretical calculations of lattice conductivity are consistent with measured experimental values, indicating the validity of the approach and premise. Given that spinodal decomposition is an efficacious and controllable metallurgical process, it offers an effective approach by lowering the lattice thermal conductivity and enhancing power factor to optimize the thermoelectric figure of merit, ZT, in this series of composition and structure on a very large scale.

5. Experimental

High-purity Pb (99.99%, American Elements), Te (99.999%, Atlantic Metals), and S (99.9%, Aldrich) were loaded into quartz ampoules at the appropriate stoichiometric quantities, flame-sealed at a residual pressure of $\sim 10^{-4}$ torr, and reacted in a high-temperature furnace to create high-purity PbTe and PbS starting materials. Samples of PbTe$_{0.7}$S$_{0.3}$ were prepared using the same method, reacted at 1100 °C for approximately 8 h, and rapidly cooled to room temperature to create a solid solution alloy

between PbTe and PbS. Certain portions of the sample were annealed for 48 h at 500 °C to facilitate spinodal decomposition.

Cylindrical samples of average dimension 8 mm diameter and 2 mm thickness were analyzed by the laser flash diffusivity technique using a Netzsch LFA 457 to measure diffusivity. Thermal conductivity was calculated from the relation $\kappa_{tot} = \alpha \rho C_p$, where κ_{tot} is the total thermal conductivity, α is the thermal diffusivity, ρ is the density as calculated from the sample dimensions and mass, and C_p is the specific heat calculated in the LFA relative to a pyroceram 9606 reference.

Electronic thermal conductivity is calculated by the Wiedemann–Franz law, $\kappa_{elec} = L_0 \ \sigma T$, where L_0 is the Lorenz number [49]. There is a considerable body of work within the field of thermoelectrics, both experimental [50–52] and theoretical [52,53], showing deviation from the universal Sommerfeld value of L_0 of 2.44×10^{-8} W Ω K^{-2}. The Lorenz number is dependent on a complex set of material properties, including elastic/inelastic scattering by point defects, electron–phonon scattering, and electron–electron scattering, all of which depend heavily on material composition and temperature [54]. Furthermore, deviations in degeneracy and band structure may also vary the Lorenz number [54]. In order to best represent the calculated values of lattice thermal conductivity, a range of Lorenz numbers were considered here, corresponding to L/L_0 values of 1, 0.9, 0.8, 0.7, 0.6, and 0.5. The resulting average values of lattice thermal conductivity will show plus and minus one standard deviation.

The samples were characterized using a JEOL 2100F transmission electron microscope. We prepared TEM samples by conventional standard methods. The samples were cut into 3 nm diameter discs by a disc cutter, and then ground, dimpled, polished, and subsequently Ar-ion milled on a stage cooled with liquid nitrogen. High-resolution images were simulated with the MACTEMPAS computer code with the following parameters as input: Spherical aberration of 2 mm, defocus spread of 8 nm, semiconvergence angle of illumination of 0.55 mrad, and a 7 nm^{-1} diameter of the objective lens' aperture.

[1] G. J. Snyder, E. S. Toberer, *Nat. Mater.* **2008**, *7*, 105.

[2] M. S. Dresselhaus, G. Chen, M. Tang, R. Yang, H. Lee, D. Wang, Z. Ren, J. Fleurial, P. Gogna, *Adv. Mater.* **2007**, *19*, 1043.

[3] B. C. Sales, *Science* **2002**, *295*, 1248.

[4] L. E. Bell, *Science* **2008**, *321*, 1457.

[5] D. M. Rowe, *CRC Handbook of Thermoelectrics*, CRC Press, Boca Raton, FL **1995**.

[6] a) J. Yang, T. Caillat, *MRS Bull.* **2006**, *31*, 224. b) G. S. Nolas, J. Poon, M. G. Kanatzidis, *MRS Bull.* **2006**, *31*, 199.

[7] a) Y. Zhang, X. Ke, C. Chen, J. Yang, P. Kent, *Phys. Rev. B* **2009**, *80*, 024304. b) O. Madelung, U. Rössler, M. Schulz, *Non-Tetrahedrally Bonded Elements and Binary Compounds I*, Springer, Berlin **2006**.

[8] a) Z. H. Dughaish, *Phys. B-Condens. Mater.* **2002**, *322*, 205. b) J. P. Heremans, C. M. Thrush, D. T. Morelli, *Phys. Rev. B* **2004**, *70*, 115334.

[9] P. W. Zhu, Y. Imai, Y. Isoda, Y. Shinohara, X. P. Jia, G. Z. Ren, G. Zou, *Mater. Trans.* **2004**, *45*, 3102.

[10] T. S. Stavitsk, V. A. Long, B. A. Efimova, *Soviet Phys. Solid State, USSR* **1966**, *7*, 2062.

[11] A. J. Mountval, G. J. Abowitz, *J. Am. Chem. Soc.* **1965**, *48*, 651.

[12] C. Wood, *Rep. Prog. Phys.* **1988**, *51*, 459.

[13] R. Venkatasubramanian, R. E. Siivola, T. Colpitts, B. Oquinn, *Nature* **2001**, *413*, 597.

[14] R. Venkatasubramanian, T. Colpitts, B. Oquinn, S. Liu, N. Ei-Masry, M. Lamvik, *Appl. Phys. Lett.* **1999**, *75*, 1104.

[15] T. C. Harman, P. J. Taylor, M. P. Walsh, B. E. LaForge, *Science* **2002**, *297*, 2229.

[16] E. Quarez, K. F. Hsu, R. Pcionek, N. Frangis, E. K. Polychroniadis, M. G. Kanatzidis, *J. Am. Chem. Soc.* **2005**, *127*, 9177.

[17] K. F. Hsu, S. Loo, F. Guo, W. Chen, J. S. Dyck, C. Uher, T. P. Hogan, M. G. Kanatzidis, *Science* **2004**, *303*, 818.

[18] P. F. R. Poudeu, J. D'Angelo, A. D. Downey, J. L. Short, T. P. Hogan, M. G. Kanatzidis, *Angew. Chem. Int. Ed.* **2006**, *45*, 3835.

[19] J. Androulakis, K. F. Hsu, R. Pcionek, H. Kong, C. Uher, J. J. Dangelo, A. D. Downey, T. P. Hogan, M. G. Kanatzidis, *Adv. Mater.* **2006**, *18*, 1170.

[20] L. Bertini, C. Stiewe, M. Toprak, S. Williams, D. Platzek, A. Mrotzek, Y. Zhang, C. Gatti, E. Muller, M. Muhammed, M. Rowe, *J. Appl. Phys.* **2003**, *93*, 438.

[21] M. S. Dresselhaus, G. Chen, M. Y. Tang, R. G. Yang, H. Lee, D. Z. Wang, Z. F. Ren, J. P. Fleurial, P. Gogna, *Adv. Mater.* **2007**, *19*, 1043.

[22] A. M. Rao, X. H. Ji, T. M. Tritt, *MRS Bull.* **2006**, *31*, 218.

[23] M. Zhou, J. F. Li, T. Kita, *J. Am. Chem. Soc.* **2008**, *130*, 4527.

[24] W. Kim, J. Zide, A. Gossard, D. Klenov, S. Stemmer, A. Shakouri, A. Majumdar, *Phys. Rev. Lett.* **2006**, *96*, 045901.

[25] T. Ikeda, L. A. Collins, V. A. Ravi, F. S. Gascoin, S. M. Haile, G. J. Snyder, *Chem. Mater.* **2007**, *19*, 763.

[26] J. Q. He, A. Gueguen, J. R. Sootsman, J. C. Zheng, L. Wu, Y. Zhu, M. G. Kanatzidis, V. P. Dravid, *J. Am. Chem. Soc.* **2009**, *131*, 17828.

[27] M. G. Kanatzidis, *Acc. Chem. Res.* **2005**, *38*, 359.

[28] J. R. Sootsman, R. J. Pcionek, H. J. Kong, C. Uher, M. G. Kanatzidis, *Chem. Mater.* **2006**, *18*, 4993.

[29] J. Androulakis, C. H. Lin, H. J. Kong, C. Uher, C. Wu, T. Hogan, B. C. Cook, T. Caillat, K. M. Paraskevopoulos, *J. Am. Chem. Soc.* **2007**, *192*, 9780.

[30] J. P. Heremans, C. M. Thrush, D. T. Morelli, *J. Appl. Phys.* **2005**, *98*, 063703.

[31] a) S. N. Girard, J. Q. He, V. P. Dravid, M. G. Kanatzidis, *Mater. Res. Soc. Symp. Proc.* **2009**, 1166. b) M. S. Darrow, W. B. White, R. Roy, *Mater. Sci. Eng.* **1969**, *3*, 289.

[32] M. J. Hytch, E. Snoeck, R. Kilaas, *Ultramicroscopy* **1998**, *74*, 131.

[33] F. C. Frank, *Physica* **1949**, *15*, 131.

[34] M. Hervieu, A. Maignan, C. Martin, N. Nguyen, B. Raveau, *Chem. Mater.* **2001**, *13*, 1356.

[35] C. H. Chen, S.-W. Cheong, *Phys. Rev. Lett.* **1996**, *76*, 4042.

[36] J. D. Gunton, M. Droz, *Introduction to the Theory of Metastable and Unstable States*, Vol. 183, Springer, Berlin **1983**.

[37] T. C. Harman, P. J. Taylor, M. P. Walsh, B. E. LaForge, *Science* **2002**, *297*, 2229.

[38] C. Chiritescu, D. G. Cahill, N. Nguyen, D. Johnson, A. Bodapati, P. Keblinski, P. Zschack, *Science* **2007**, *315*, 351.

[39] J. Callaway, H. C. Von Baeyer, *Phys. Rev.* **1960**, *120*, 1149.

[40] D. T. Morelli, J. P. Heremans, *Phys. Rev. B* **2002**, *66*, 195 304.

[41] E. F. Steigmeier, B. Abeles, *Phys. Rev.* **1964**, *136*, A1149.

[42] L. Yang, J. Wu, L. Zhang, *Chin. Phys.* **2004**, *13*, 0516.

[43] G. Chen, C. Dames, D. Song, C. T. Harris, *Thermal Conductivity 27/Thermal Expansion 15* (Ed: H. Huang, W. Porter), DEStech Publications, Lancaster, USA **2004**, p. 263.

[44] G. Chen, T. Zeng, T. D. Borca-Tascius Song, *Mater. Sci. Eng.* **2000**, *292*, 155.

[45] J. Zou, D. Kotchetkov, A. A. Balandin, D. I. Florescu, F. H. Pollak, *J. Appl. Phys.* **2002**, *92*, 2534.

[46] W. Kim, S. L. Singer, A. Majumdar, J. M. O. Zide, D. Klenov, A. C. Gossard, S. Stermer, *Nano Lett.* **2008**, *8*, 2097.

[47] W. Kim, A. Majumdar, *J. Appl. Phys.* **2006**, *99*, 084306.

[48] N. Mingo, D. Hauser, N. P. Kobayashi, M. Plissonnier, A. Shakouri, *Nano Lett.* **2009**, *9*, 711.

[49] C. Kittel, *Introduction to Solid State Physics*. 1st ed., John Wiley and Sons, Inc., New York **1953**, p. 245.

[50] Y. I. Ravich, I. A. Smirnov, V. V. Tikhonov, *Soviet Phys.–Semicond.* **1967**, *1*, 163.

[51] G. T. Alekseeva, I. N. Dubrovskaya, B. A. Efimova, *Soviet Phys.–Semicond.* **1973**, *7*, 157.

[52] V. I. Tamarchenko, Y. I. Ravich, L. Y. Morgovskii, I. N. Dubrovskaya, *Soviet Phys.–Solid State* **1970**, *11*, 2599.

[53] V. M. Muzhdaba, S. S. Shalyt, *Soviet Phys.–Solid State* **1967**, *8*, 2997.

[54] G. S. Kumar, G. Prasad, R. O. Pohl, *J. Mater. Sci.* **1993**, *28*, 4261.